Coal-derived two-dimensional MNb_2O_6(M=Mn, Fe, Co)/C hybrids with superior lithium storage performance

Yang Zhang [a]*, Ziyun Ma [a], Yanjun Cai [a], Qingrong Kong [a], Jiayao Zhu [a], Zhengen Sun [a] and Lang Liu [b,]*

([a] *College of Chemistry and Chemical Engineering, Xinjiang Key Laboratory of Energy Storage and Photoelectrocatalytic Materials, Xinjiang Normal University, Urumqi, 830054, Xinjiang, China*)

([b] *State Key Laboratory of Chemistry and Utilization of Carbon Based Energy Resources, College of Chemistry, Xinjiang University, Urumqi, 830017, Xinjiang, China*)

**Corresponding author: Yang Zhang, Lang Liu*

E-mail: zyangxy@163.com, liulang@xju.edu.com

Materials

Coal was produced in Kuche, relative analysis on the coal has been reported in previous literature [1]. Niobium(V) oxide (Nb_2O_5, 99%) was purchased from the Aladdin Reagent Company. Manganese (II) chloride, ferric nitrate, and cobaltous nitrate (AR grade) were purchased from Tianjin Zhiyuan Chemical Reagent Co., Ltd. Sulfuric acid (H_2SO_4, 98%), nitric acid (HNO_3, 63%), and (HCl, 37%) were purchased from Chengdu Cologne Chemicals Co., Ltd. Absolute ethanol (AR grade) was purchased from Tianjin Kemeng Chemical Industry and Trade Co., Ltd. All these reagents were used without purification.

Characterization

Material composition was characterized by X-ray diffraction (XRD; Bruker D8/Cu Kα radiation). Morphology analysis was tested by employing Hitachi's field-emission scanning electron microscopy (SEM, S-4800) and transmission electron microscopy (TEM) and high-resolution transmission electron microscope (HRTEM, JEOL JEM-2100F). Thermogravimetric analysis (TGA) was carried out by using Netzsch STA 449C in air atmosphere from room temperature to 800 ^{o}C with a heating rate of 10 ^{o}C min^{-1}. Brunauer-Emmett-Teller (BET) specific surface area and pore structure analysis (DFT method) of the samples were measured by nitrogen adsorption/desorption with an Autosorb-iQ Pressure Sorption Analyzer (Quantachrome Instruments USA) at 77 K.

Electrochemical Characterization

The working electrodes (half-cells) were obtained through the following procedures: mixing the active materials (80 wt%), acetylene black (10 wt%), and polyvinylidene fluoride binder (10 wt%), followed by dropwise addition of N-methyl-2-pyrrolidone (NMP) to form a homogeneous slurry, which was uniformly spread onto a copper foil, then the coated copper foil was dried overnight under vacuum at 110 °C. The assembly of cells was operated in an argon-filled glovebox with suitable water/oxygen concentrations, using lithium metal as the counter electrode，Celgard 2400 membrane as the separator, and $LiPF_6$ (1 M) in mixed solvents of ethyl carbonate/diethyl carbonate (1:1, v/v) as the electrolyte. Cyclic voltammetry curves were obtained on a CHI-760C workstation with a sweep rate of 0.1 mV s^{-1}. Galvanostatic charge and discharge (GCD) measurements were conducted on a Land (CT2001A China) at 0.01-3.00 V (versus Li^+/Li). Electrochemical impedance spectra (EIS) behaviors were gained within the frequency scope of 100 kHz to 10 mHz. All tests were conducted at room temperature, and the mass loading of the actively materials was about 0.8 mg cm^{-2}.

For the preparation of full cell battery, FeNO/C was used as anode, commercial $LiFePO_4$ was employed as cathode, and the electrolyte was commercially purchased (Guangzhou Tianci Advanced Materials Co., Ltd.). Specifically, $LiFePO_4$, N-carbon black, and polyvinylidene fluoride were evenly mixed in a mass ratio of 80:10:10, adding NMP to obtain a homogeneous slurry. Then the slurry was uniformly coated on the Al foil and dried overnight in a vacuum oven, the loading mass of $LiFePO_4$ is about four times of FeNO/C. Before the assembly of full battery, the half-battery was pre-lithiated at 0.1 A g^{-1} for three cycles, and disassembled in the Ar glovebox. The anode electrode was rinsed with commercial electrolyte, and then reassembled with the pre-prepared cathode in the Ar glovebox. The obtained full batteries were operated in the

potential range of 1.0-4.5 V, and the specific capacity was calculated based on the cathode material.

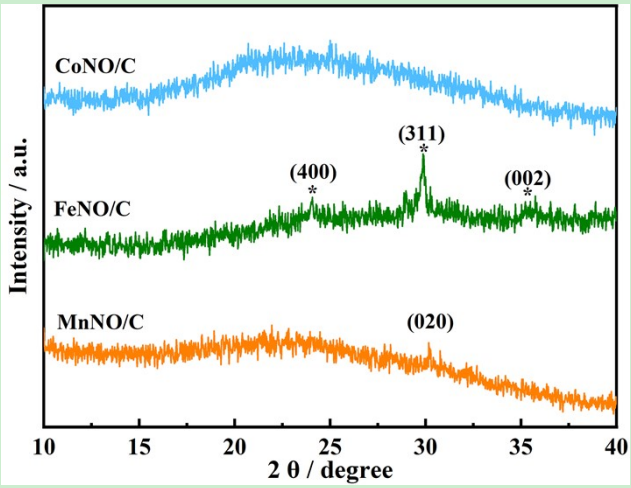

Fig. S1. XRD patterns of MnNO/C, FeNO/C, and CoNO/C electrodes after 600 cycles.

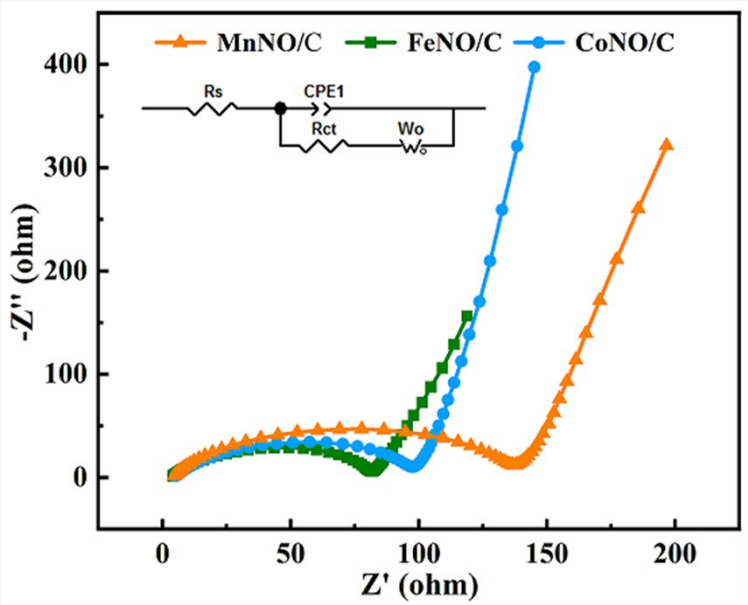

Fig. S2. Electrochemical impedance spectra (EIS) of MnNO/C, FeNO/C, and CoNO/C.

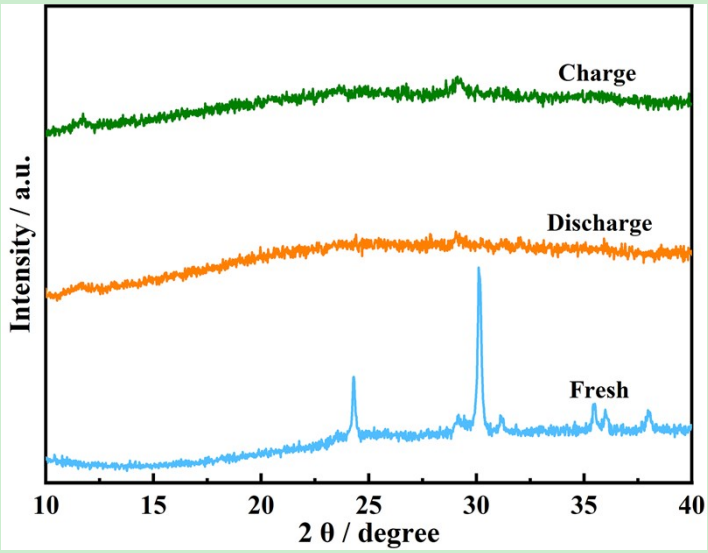

Fig. S3. *Ex situ* XRD patterns of CoNO/C after three cycles.

Table S1. Comparison on the Li^+ diffusion coefficient of M-Nb-O-based anode materials in the reported literature.

Materials	D_{Li^+}(cm^2/s, lithiation)	D_{Li^+}(cm^2/s, delithiation)	Test method	Ref
$CrNb_{11}O_{29}$ nanorods	1.51×10^{-13}	3.57×10^{-13}	CV	[2]
TNO@C	2.39×10^{-12}	2.13×10^{-12}	CV	[3]
$TiNb_6O_{17}$	1.33×10^{-12}	1.59×10^{-12}	CV	[4]
N-doped $TiNb_{24}O_{62}$/C nanowires	4.11×10^{-12}	3.89×10^{-12}	CV	[5]
$GaNb_{11}O_{29}$@C	4.30×10^{-13}	3.67×10^{-13}	CV	[6]
$BaNb_{3.6}O_{10}$ nanowires	2.36×10^{-12}	2.79×10^{-12}	CV	[7]
$Mg_2Nb_{34}O_{87}$	3.23×10^{-13}	6.36×10^{-13}	CV	[8]
$AlNb_{11}O_{29}$	1.12×10^{-13}	2.39×10^{-13}	CV	[9]
Zn2Nb34O87				
$AgNb_{13}O_{33}$	4.03×10^{-12}		CV	[10]
$ZrNb_{14}O_{37}$ nanowire	4.63×10^{-14}		CV	[11]
porous $ZrNb_{24}O_{62}$ nanowires	2.47×10^{-13}		EIS	[12]
$CrNb_{49}O_{124}$ nanotube	5.29×10^{-13}		EIS	[13]

N-doped $TiNb_2O_7$@C	8.81×10^{-18}		EIS	[14]
$TiNb_2O_7$/C	4.11×10^{-12}		EIS	[15]
Popcorn like Nb_2O_5	1.68×10^{-20}		EIS	[16]
$FeNb_{11}O_{29}$ nanotubes	2.51×10^{-12}		EIS	[17]
$Fe_{0.5}Nb_{24.5}O_{62-x}$@C nanowires	4.03×10^{-13}		EIS	[18]
$TiNb_2O_7$@N–C	6.07×10^{-11}		EIS	[19]
$Cu_2Nb_{34}O_{87}$	3.1×10^{-13}	3.9×10^{-13}	GITT	[20]
$Zn_2Nb_{34}O_{87}$ nanofibers	6.6×10^{-12}	6.1×10^{-12}	GITT	[21]
$V_3Nb_{17}O_{50}$ submicron-sized rods	2.75×10^{-12}	2.63×10^{-12}	GITT	[22]
V^{5+}-doped $TiNb_2O_7$ microspheres	$\sim 4.1 \times 10^{-13}$	$\sim 5.5 \times 10^{-13}$	GITT	[23]
Microsized $MoNb_{12}O_{33}$ particles	2.9×10^{-14}	4.8×10^{-14}	GITT	[24]
partially reduced $TiNb_{24}O_{62}$	7.4×10^{-12} (average)		GITT	[25]
$BaNb_{3.6}O_{10}$	1.5×10^{-12}	1.8×10^{-12}	GITT	[26]
$Mg_2Nb_{34}O_{87}$	5.0×10^{-13} (average)		GITT	[27]
$AlNb_{11}O_{29}$	1.22×10^{-13} (average)		GITT	[28]
$TiNb_2O_7$/C	1.41×10^{-13}	1.52×10^{-13}	GITT	[29]
$FeNb_2O_6$/C	**1.4×10^{-10}**	**6.3×10^{-11}**	**GITT**	**This work**

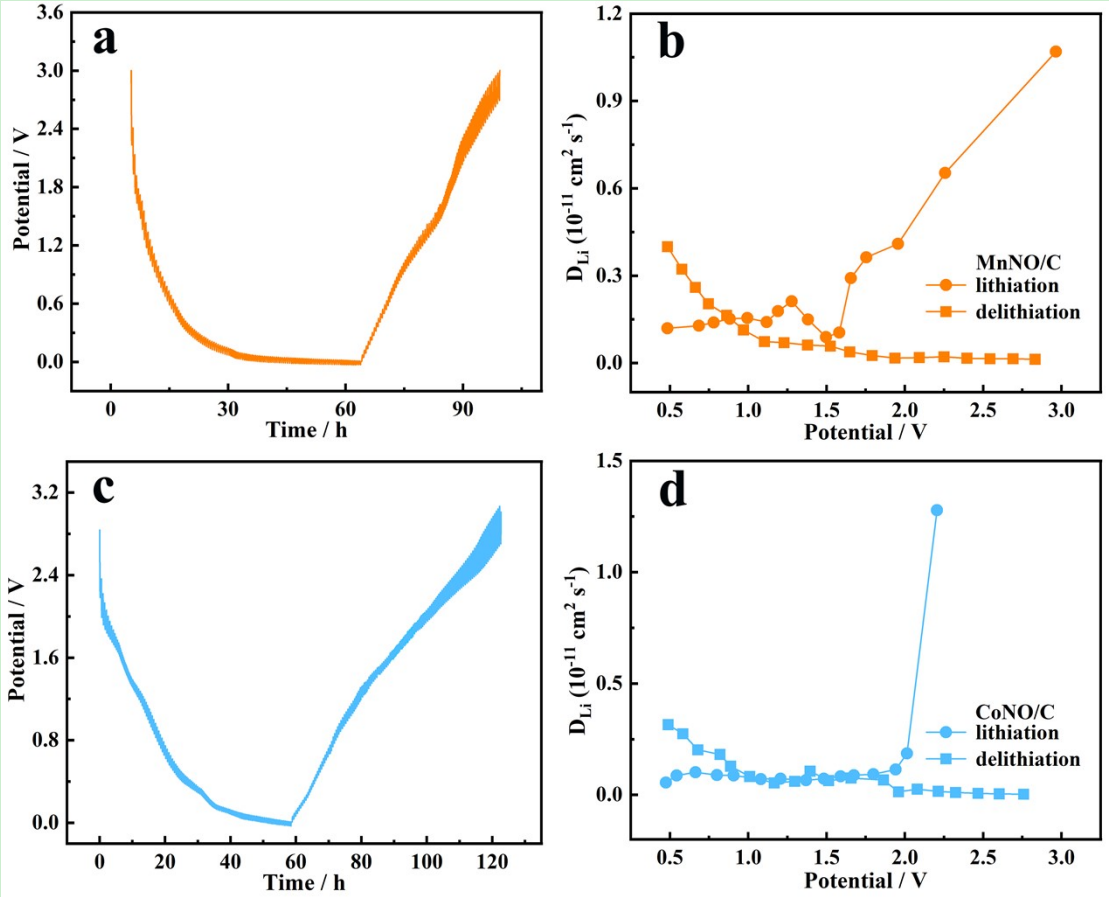

Fig. S4. GITT curves (a, c) and varied D_{Li}^+ (b, d) of MnNO/C and CoNO/C.

Similar to FeNO/C, the Li^+ diffusion coefficient (D_{Li}^+) of MnNO/C and CoNO/C was also calculated using a GITT test, and the equation for the diffusion coefficients have been described in the main text. As shown in Fig. S4, during the lithiation process, the D_{Li}^+ value of MnNO/C, and CoNO/C ranged from 1.1×10^{-11} to 1.2×10^{-12} and 1.3×10^{-11} to 5.5×10^{-13} cm^2 s^{-1}, with an average D_{Li}^+ of 2.7×10^{-12} and 1.7×10^{-12} cm^2 s^{-1}, respectively. And the value during the delithiation process varied in the ranges of 4.0×10^{-12} to 1.3×10^{-13} and 3.2×10^{-12} to 4.2×10^{-14} cm^2 s^{-1}, with an average D_{Li}^+ of 1.0×10^{-12} and 8.9×10^{-13} cm^2 s^{-1}, respectively.

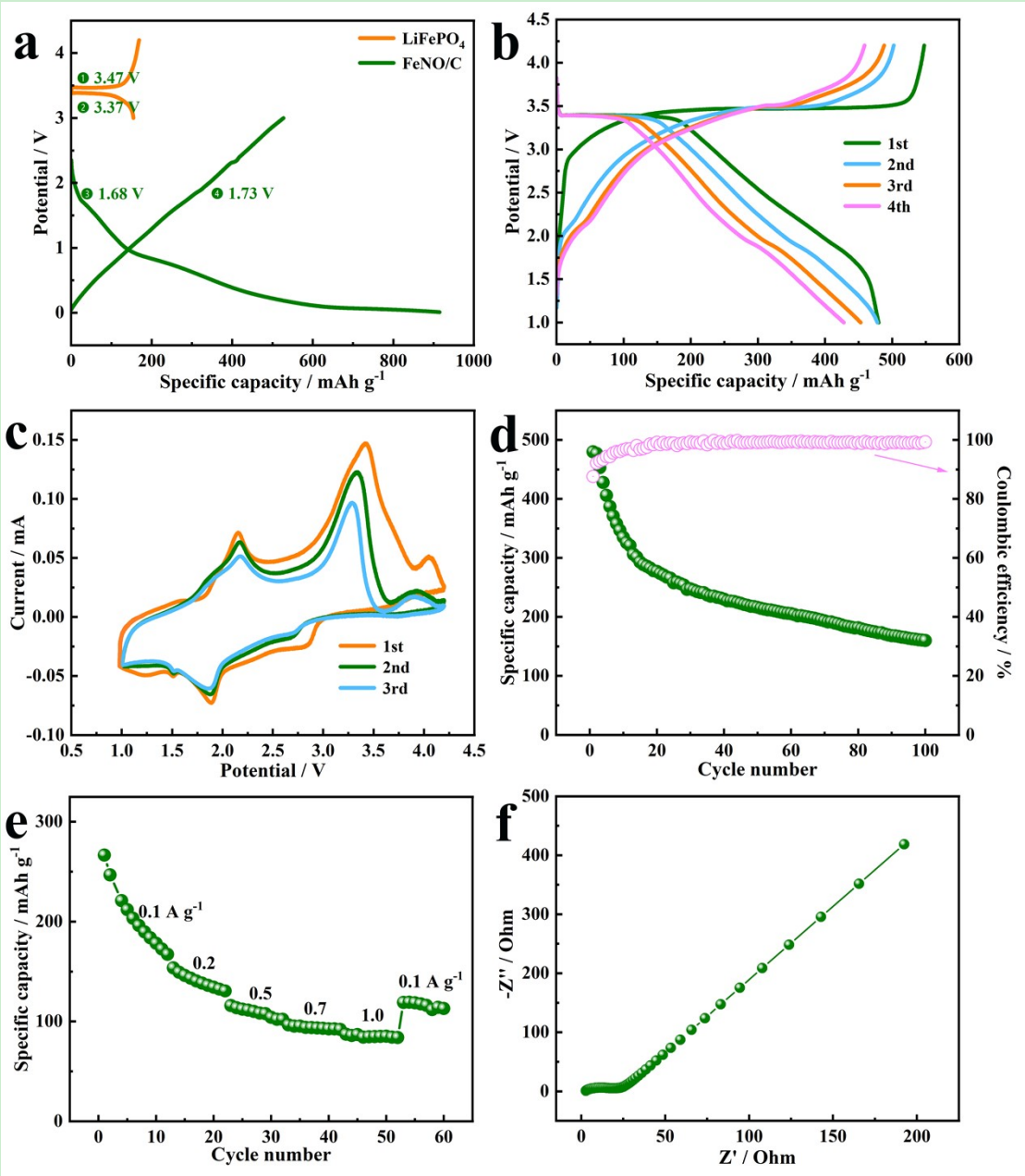

Fig. S5. Electrochemical properties of $LiFePO_4$‖FeNO/C full battery: initial GCD curves of FeNO/C‖Li and $LiFePO_4$‖Li half batteries at 0.1 A g^{-1} (a), GCD curves of the full battery at 0.1 A g^{-1} (b), CV curves (c), cyclic performance (d), rate performance (e), and EIS (f).

The excellent cycling performance, favorable rate performance, and competitive diffusion kinetics of FeNO/C hybrid nanosheets have inspired the exploration in the field of full batteries, whose capacity can be calculated on the basis of the mass of the cathode active materials. The assembly of the half and full batteries have been described

in the experimental characterization section. As shown in Fig. S5a, the GCD curves of commercial $LiFePO_4$ cathode (orange) shows plateaus at 3.47 and 3.37 V, relate to the redox of Fe^{2+} and Fe^{3+}, and the plateaus appeared at 1.68 and 1.73 V for FeNO/C anode (green) can be ascribed to the valence change of Nb^{5+}/Nb^{4+} pair. Correspondingly, the specific capacity of $LiFePO_4$ cathode is 154.6 mAh g^{-1} at 0.1 A g^{-1} for the initial cycle, while FeNO/C reaches 914.5 mAh g^{-1}. Fig. S5b shows the GCD curves of the full battery for the initial four cycles, which reveals an initial charge/discharge specific capacity of 547.6 and 479.7 mAh g^{-1}, respectively, with a coulombic efficiency of 87.6%, and the capacity loss can be attributed to the formation of SEI film and occurrence of irreversible reactions. During the following three cycles, the battery illustrates a charge/discharge capacity of 502.2/477.9, 488/453, and 458.8/ 427.9 mAh g^{-1}, respectively. In order to further investigate the electrochemical performance of $LiFePO_4$‖FeNO/C full battery, CV test (Fig. S5c) was conducted at 0.1 mV s^{-1}. Similar to the plateaus appeared in the half cells (Fig. S5a), the redox peaks at 3.43 and 2.86 V can be attributed to the (de)intercalation of Li^+ in $LiFePO_4$, and the peaks around 2.15 and 1.88 V are related to the redox reaction in $FeNb_2O_6$. Cyclic performance (Fig. S5d) of the full battery shows that the discharge specific capacity presents a gradual decrease trend during cycling, which was caused by the continuous deposition of Li^+, leading to a decrease in the lithium metal available for reuse [30], and the discharge specific capacity of the full battery is maintained at 160 mAh g^{-1} with an average Coulombic efficiency of 98.4% after 100 cycles. The rate capability (Fig. S5e) shows that the battery displays a specific capacity of 203.3, 146.1, 112.2, 95.3 and 86.7 mAh g^{-1} at 0.1, 0.2, 0.5, 0.7 and 1 A g^{-1}, respectively, and basically return to the initial level after cycling at 1 A g^{-1}, demonstrate its favorable structural stability. EIS analysis (Fig. S5f) reveals a lower charge transfer resistance (R_{ct} = 14.1 Ω), and large slope in the high-frequency region indicate that the battery has a low resistance and fast lithium ion diffusion rate.

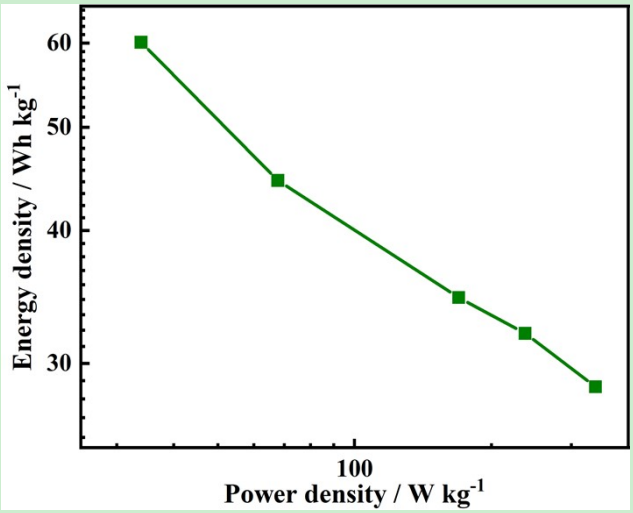

Fig. S6. Ragone plot of the $LiFePO_4$‖FeNO/C full battery.

Finally, the relationship between the energy density and power density of the $LiFePO_4$‖FeNO/C full battery can be calculated from the Rangone curve (Fig. S6), which shows that the energy density of the full battery decreases with the increase of the power density, and the power and energy densities are 33.9 W kg^{-1} and 60.1 Wh kg^{-1} at 0.1 A g^{-1}, respectively.

References

[1] S. Gao, Y. Tang, L. Wang, L. Liu, D. Jia, Z. Zhao, NiFe nanoalloys in-situ immobilized on coal based activated carbons through one-step pyrolysis as magnetically recoverable catalysts for reduction of 4-nitrophenol, J. Alloys Compd. 702 (2017) 531-537.

[2] Q. Fu, X. Liu, J. Hou, Y. Pu, C. Lin, L. Yang, X. Zhu, L. Hu, S. Lin, L. Luo, Y. Chen, Highly conductive $CrNb_{11}O_{29}$ nanorods for use in high-energy, safe, fast-charging and stable lithium-ion Batteries, J. Power Sources 397 (2018) 231-239.

[3] H. Lyu, J. Li, T. Wang, B. Thapaliya, S. Men, C. Jafta, R. Tao, X. Sun, S. Dai, Carbon coated porous titanium niobium oxides as anode materials of lithium-ion batteries for extreme fast charge applications, ACS Appl. Energ. Mater. 3 (2020) 5657-5665.

[4] Y. Yuan, H. Yu, X. Cheng, R. Zheng, T. Liu, N. Peng, N. Long, Shui, M, J. Shu, Preparation of $TiNb_6O_{17}$ nanospheres as high-performance anode candidates for lithium-ion storage, Chem. Eng. J. 374 (2019) 937-946.

[5] H. Yu, X. Cheng, H. Zhu, R. Zheng, T. Liu, J. Zhang, M. Shui, Y. Xie, J. Shu, Deep insights into kinetics and structural evolution of nitrogen-doped carbon coated $TiNb_{24}O_{62}$ nanowires as high-performance lithium container, Nano Energy 54 (2018) 227-237.

[6] Z. Wang, R. Zheng, Y. Li, H. Yu, J. D. Zhang, X. Zhang, W. Bi, M. Shui, J. Shu, Synthesis and characterization of $GaNb_{11}O_{29}$@C for high-performance lithium-ion battery. Ceram. Int. 46 (2020) 5913-5919.

[7] X. Cheng, S. Qian, H. Yu, H. Zhu, Y. Xie, R. Zheng, T. Liu, M. Shui, J. Shu, $BaNb_{3.6}O_{10}$ nanowires with superior electrochemical performance towards ultrafast and highly stable lithium storage, Energy Storage Mater. 16 (2019) 400-410.

[8] X. Zhu, Q. Fu, L. F. Tang, C. Lin, J. Xu, G. Liang, R. Li, L. J. Luo, Y. Chen, $Mg_2Nb_{34}O_{87}$ porous microspheres for use in high-energy, safe, fast-charging, and

stable lithium-ion batteries, ACS Appl. Mater. Interface 10 (2018) 23711-23720.

[9] X. Lou, R. Li, X. Zhu, L. Luo, Y. Chen, C. Lin, H. Li, X. S Zhao, New anode material for lithium-ion batteries: aluminum niobate ($AlNb_{11}O_{29}$), ACS Appl. Mater. Interface 11 (2019) 6089-6096.

[10] Z. Chen, X. Cheng, W. Ye, R. Zheng, H. Zhu, H. Yu, N. Long, M. Shui, J. Shu, $AgNb_{13}O_{33}$: a new anode material with high energy storage performance, Chem. Eng. J. 366 (2019) 246-253.

[11] Y. Li, R. Zheng, H. Yu, X. Cheng, T. T. Liu, N. Peng, J. Zhang, M. Shui, J. Shu, Observation of $ZrNb_{14}O_{37}$ nanowires as a lithium container via in situ and ex situ techniques for high-performance lithium-ion batteries, ACS Appl. Mater. Interface 11 (2019) 22429-22438.

[12] C. Yang, Y. Zhang, F. Lv, C. Lin, Y. Liu, K. Wang, J. Feng, X. Wang, Y. Chen, J. B. Li, S. Guo, Porous $ZrNb_{24}O_{62}$ nanowires with pseudocapacitive behavior achieve high-performance lithium-ion storage, J. Mater. Chem. A 5 (2017) 22297-22304.

[13] W. Ye, H. Yu, X. Cheng, H. Zhu, R. Zheng, T. Liu, N. Long, M. Shui, J. Shu, Constructing hollow nanofibers to boost electrochemical performance: insight into kinetics and the Li storage mechanism for $CrNb_{49}O_{124}$, ACS Appl. Mater. Interface 2 (2019) 2672-2679.

[14] J. Gao, X. Cheng, S. Lou, X. Wu, F. Ding, P. Zuo, Y. Ma, C. Du, Y. Gao, G. Yin, Surface nitrided and carbon coated $TiNb_2O_7$ anode material with excellent performance for lithium-ion batteries, J. Alloys. Compd. 835 (2020) 155241-115248.

[15] Y. Yang, Y. Yue, L. Wang, X. Cheng, Y. Hu, Z. Yang, R. Zhang, B. Jin, R. Sun, Facile synthesis of mesoporous $TiNb_2O_7$/C microspheres as long-life and high-power anodes for lithium-ion batteries, Int. J. Hydrogen Energ. 45 (2020) 12583-12592.

[16] S. Shen, S. Zhang, X. Cao, S. Deng, G. Pan, Q. Liu, X. Wang, X. Xia, J. Tu, Popcorn-like niobium oxide with cloned hierarchical architecture as advanced anode for solid-state lithium ion batteries, Energy Storage Mater. 25 (2020) 695-701.

[17] R. Zheng, S. Qian, X. Cheng, H. Yu, N. Peng, T. Liu, J. Zhang, M. Xia, H. Zhu, J. Shu, $FeNb_{11}O_{29}$ nanotubes: superior electrochemical energy storage performance and operating mechanism, Nano Energy 58 (2019) 399-409.

[18] R. Zheng, Y. Li, H. Yu, T. Liu, M. Xia, X. Zhang, N. Peng, J. Zhang, Y. Bai, J. Shu, Rational construction and decoration of $Fe_{0.5}Nb_{24.5}O_{62-x}$@C nanowires as superior anode material for lithium storage, Chem. Eng. J. 384 (2020) 123314-1233121.

[19] G. Liu, X. Liu, X. Li, W. Zhang, S. Li, Y. Ding, B. Jin, X. Liu, Y. Luo, Three-dimensional hierarchical urchin-like $TiNb_2O_7$ microspheres encapsulated in N-doped carbon for high-rate lithium storage, J. Colloid Interf. Sci. 686 (2025) 1033-1042.

[20] L. Yang, X. Zhu, X. Li, X. Zhao, K. Pei, W. You, X. Li, Y. Chen, C. Lin, R. Che, Conductive copper niobate: superior Li^+-storage capability and novel Li^+-transport mechanism, Adv. Energy Mater. 9 (2019) 1902174-1902183.

[21] X. Zhu, H. Cao, R. Li, Q. Fu, G. Liang, Y. Chen, L. Luo, C. Lin, X. Zhao, Zinc niobate materials: crystal structures, energy-storage capabilities and working mechanisms, J. Mater. Chem. A 7 (2019) 25537-25547.

[22] Q. Fu, X. Zhu, R. Li, G. Liang, L. Luo, Y. Chen, Y. Ding, C. Lin, K. Wang, X. Zhao, A low-strain $V_3Nb_{17}O_{50}$ anode compound for superior Li^+ storage, Energy Storage Mater. 30 (2020) 401-411.

[23] K. Liu, J. Wang, J. Yang, D. Zhao, P. Chen, J. Man, X. Yu, Z. Wen, J. Sun, Interstitial and substitutional V^{5+}-doped $TiNb_2O_7$ microspheres: a novel doping way to achieve high-performance electrodes, Chem. Eng. J. 407 (2021) 127190-

127202.

[24] X. Zhu, J. Xu, Y. Luo, Q. Fu, G. Liang, L. Luo, Y. Chen, C. Lin, X. Zhao, $MoNb_{12}O_{33}$ as a new anode material for high-capacity, safe, rapid and durable Li^+ storage: structural characteristics, electrochemical properties and working mechanisms, J. Mater. Chem. A 7 (2019) 6522-6532.

[25] T. Jiang, S. Ma, J. Deng, T. Yuan, C. Lin, M. Liu, Partially reduced titanium niobium oxide: a high-performance lithium-storage material in a broad temperature range, Adv. Sci. 9 (2022) 2105119-2105128.

[26] C. Lu, P. Kulkarni, S. Balaji, P. Kumar, Exploration of electrochemical and lithium transport properties of $BaNb_{3.6}O_{10}$ as an anode material for lithium-ion batteries, J. Alloy. Compd. 830 (2020) 154306-154313.

[27] C. Lv, C. Lin, X. Zhao, Enhancing low-temperature electrochemical kinetics and high-temperature cycling stability by decreasing ionic packing factor, eScience 3 (2023) 100179-100189.

[28] A. Reach, A. Zohar, M. Wright, T. Li, R. Seshadri, Rapid microwave preparation of $AlNb_{11}O_{29}$ and $Ti_2Nb_{10}O_{29}$ Wadsley-Roth lithium-ion anode compounds from parent oxides, ACS Appl. Energy Mater. 8 (2025) 7714-7721.

[29] N. Kosova, D. Tsydypylov, Effect of mechanical activation and carbon coating on electrochemistry of $TiNb_2O_7$ anodes for lithium-ion batteries, Batteries 8 (2022) 52-63.

[30] X. Han, E. Ang, C. Zhou, F. Zhu, X. Zhang, H. Geng, X. Cao , J. Zheng, H. Gu, Dual carbon-confined Sb_2Se_3 nanoparticles with pseudocapacitive properties for high-performance lithium-ion half/full batteries, Dalton Transactions 50 (2021) 6642-6649.